HHS Public Access

Author manuscript

Nat Energy. Author manuscript; available in PMC 2024 January 19.

Published in final edited form as:

Nat Energy. 2023 December ; 8(12): 1345–1354. doi:10.1038/s41560-023-01361-1.

Direct in situ measurements of electrical properties of solid–electrolyte interphase on lithium metal anodes

Yaobin Xu[1,9], **Hao Jia**[2,9], **Peiyuan Gao**[3], **Diego E. Galvez-Aranda**[4,5], **Saul Perez Beltran**[4], **Xia Cao**[2], **Phung M. L. Le**[2], **Jianfang Liu**[6], **Mark H. Engelhard**[1], **Shuang Li**[1], **Gang Ren**[6], **Jorge M. Seminario**[4,5,7], **Perla B. Balbuena**[4,7,8], **Ji-Guang Zhang**[2], **Wu Xu**[2], **Chongmin Wang**[1]

[1]Environmental Molecular Sciences Laboratory, Pacific Northwest National Laboratory, Richland, WA, USA.

[2]Energy and Environment Directorate, Pacific Northwest National Laboratory, Richland, WA, USA.

[3]Physical and Computational Sciences Directorate, Pacific Northwest National Laboratory, Richland, WA, USA.

[4]Department of Chemical Engineering, Texas A&M University, College Station, TX, USA.

[5]Department of Electrical and Computer Engineering, Texas A&M University, College Station, TX, USA.

[6]The Molecular Foundry, Lawrence Berkeley National Laboratory, Berkeley, CA, USA.

[7]Department of Materials Science and Engineering, Texas A&M University, College Station, TX, USA.

[8]Department of Chemistry, Texas A&M University, College Station, TX, USA.

[9]These authors contributed equally: Yaobin Xu, Hao Jia.

Abstract

The solid–electrolyte interphase (SEI) critically governs the performance of rechargeable batteries. An ideal SEI is expected to be electrically insulative to prevent persistently parasitic reactions between the electrode and the electrolyte and ionically conductive to facilitate Faradaic reactions of the electrode. However, the true nature of the electrical properties of the SEI remains

Correspondence and requests for materials should be addressed to Jorge M. Seminario, Perla B. Balbuena, Wu Xu or Chongmin Wang. seminario@tamu.edu; balbuena@tamu.edu; wu.xu@pnnl.gov; chongmin.wang@pnnl.gov.

Author contributions

C.W. and Y.X. conceived the project and designed the experiments with suggestions from W.X. and H.J. Y.X. collected and analysed experimental data for in situ TEM and cryo-TEM studies and drafted the paper under the direction of C.W. and W.X. H.J. performed the electrochemical measurements. P.G. performed the AIMD calculation of bulk electrolytes. D.E.G.-A. and J.M.S. performed the SEI composition analyses, the molecular orbital electronic structure calculations and the current-voltage characteristics of the SEI samples. S.P.B. and P.B.B. performed hybrid AIMD combined with reactive force field simulations. J.L. and G.R. carried out three-dimensional reconstruction. X.C. conducted battery cycling tests. P.M.L.L. and J.-G.Z. helped with interpretation of the electrochemical data. M.H.E. collected XPS data. S.L. prepared the W STM tip. Y.X., H.J., W.X. and C.W. co-wrote the original paper. All authors discussed the results and edited the paper.

Supplementary information The online version contains supplementary material available at https://doi.org/10.1038/s41560-023-01361-1.

Competing interests

The authors declare no competing interests.

hitherto unclear due to the lack of a direct characterization method. Here we use in situ bias transmission electron microscopy to directly measure the electrical properties of SEIs formed on copper and lithium substrates. We reveal that SEIs show a voltage-dependent differential conductance. A higher rate of differential conductance induces a thicker SEI with an intricate topographic feature, leading to an inferior Coulombic efficiency and cycling stability in Li||Cu and Li||$LiNi_{0.8}Mn_{0.1}Co_{0.1}O_2$ cells. Our work provides insight into the targeted design of the SEI with desired characteristics towards better battery performance.

Functioning of a rechargeable battery depends on the synergy of three major components in the cell: anode, electrolyte and cathode. The electrolyte, in either solid state or liquid state, is sandwiched between the cathode and the anode to facilitate ion transport[1-3]. The interface between electrolyte and electrode is not atomically sharp; instead, electron transfer across the interface leads to the formation of an interphasial layer, which is termed a solid–electrolyte interphase (SEI) layer[1,4-7]. The characteristics of the SEI layer, including chemical, structural, morphological and mechanical properties[4,8-10], determine a series of key properties of rechargeable batteries, such as active ion inventory, cycle life, rate capability and temperature-dependent performance of a rechargeable battery[2,3,5,11,12]. For better battery performances, the SEI is expected to possess three ideal characteristics: electrically insulative, ionically conductive and constant thickness[5,6]. These three characteristics are interactively correlated. Typically, the SEI thickness is controlled by the electrical properties of the SEI. The thickness of the SEI continuously increases during charge–discharge cycling and shelf storage, indicating that the SEI does not behave as an electrical insulator[1,5,12]. Electronic structure calculations indicate that certain SEI components and their grain boundaries, in contrast with their crystalline counterparts, are prone to electron leakage through the SEI layer[13-18], leading to continued SEI thickening. A thick SEI increases the ion conduction length and consequently the ionic resistance, deteriorating the kinetic properties of batteries[11,12,14]. In addition, the SEI growth also consumes active ions and electrolytes in the batteries, leading to capacity decay, short cycle life and calendar life of the batteries. Although different mechanisms based on mathematical and theoretical models have been proposed to account for the electron leakage behaviour of the SEI and consequently to explain the continuous growth of the SEI[6,14,19-25], such as solvent diffusion[20,21], electron conduction[20,21,23,26], electron tunnelling[27] and Li-interstitial diffusion[22], the transport mechanism behind these phenomena is still under debate and not identified directly by experiment.

Despite the critical importance of the electrical properties of the SEI, quantitative measurement of this parameter remains unsolved due to the lack of a proper and reliable method. The four-point Hebb–Wagner polarization and electrochemical impedance spectroscopy methods for mixed ionic–electronic conductors cannot be readily applied to quantify the electrical conductivity of the SEI[28-30], because the SEI is not only highly air sensitive but also very thin, which is beyond the high spatial resolution of the method. Scanning probe microscopy inside a glovebox or scanning electron microscopy could solve the air-sensitive issue[31,32]. However, the scanning probe method is based on the principle of touching the top surface of the sample, without any information from the top surface to the counter electrode. Adhering to the nature of this limitation, the thickness of the SEI layer at

the measuring site cannot be in situ measured. Consequently, it is hard to directly correlate the microstructure and chemical information of the SEI with the measured resistivity. In spite of the lack of concrete experimental evidence, it is widely assumed that an SEI layer behaves as an insulator, as such an assumption helps to interpret, to some degree, the electrochemical performances of rechargeable batteries[4]. In essence, for all types of cell chemistry that are enabled by the SEI, the electrical and ionic properties of the SEI remain the most challenging mystery, leading to a range of behaviours of rechargeable batteries being uninterpreted.

In this Article, we describe an in situ bias transmission electron microscopy (TEM) approach to directly measure the electrical properties of SEI layers grown on copper (Cu) and lithium (Li) substrates, revealing the electrical characteristics of the SEI in terms of current (I)–voltage (V) relationship, differential conductance, critical field strength and bandgap. We unveil that the $I-V$ characteristics of SEIs resemble certain electrical conductance, rather than electrical insulators as assumed in most studies. The SEI with a higher rate differential conductance tends to exhibit a greater thickness and more complex topographic features, consequently leading to an inferior electrochemical performance. The work highlights the governing role of electrical properties of the SEI layer and their tuning towards the enhanced performance of an electrochemical cell.

Electrical properties of SEI layer and battery performance

We integrated in situ TEM with scanning tunnelling microscopy (STM) technique to measure the electrical properties of SEIs on Cu and Li, as illustrated in Fig. 1 and detailed in Supplementary Methods and Supplementary Figs. 1-7. A STM tungsten (W) nanoprobe with atomically clean surface was used as the counter electrode (Supplementary Fig. 3), which was manipulated by the piezo system with three-axis nanometre-scale control. As ion-blocking Cu and W electrodes are used, the measured $I-V$ data directly reflect the electron transport behaviour of the SEI. It should be noted that this measurement with two blocking electrodes does not exactly resemble a real Wagner–Hebb polarization measurement but rather provides an upper limit value of the electrical conductivity[28,33,34]. As the SEI is very sensitive to electron beam[35-38], we performed the $I-V$ measurements at very low magnification of electron dose rate of $1\,e^{-}\,Å^{-2}\,s^{-1}$ to avoid electron-beam-induced damage to the SEI and did $I-V$ curve measurement calibration to make sure the experimental results are repeatable and credible (Supplementary Figs. 8-14 and Supplementary Notes 1-3). Besides, we built Li–electrolyte interface models (Fig. 2a) to investigate the SEI structure using hybrid ab initio molecular dynamics (AIMD) simulation (Fig. 2b) and subsequently calculate the electron transport in the SEI in terms of $I-V$ curve (Fig. 2c). To systematically study different SEIs, Li bis(fluorosulfonyl) imide (LiFSI) and 1,2-dimethoxyethane (DME) were chosen to make four electrolytes with designed microscopic solvation structures[39,40]: (1) a low-concentration electrolyte (LCE) comprised of 1 M LiFSI in DME with a molar ratio of 1:9; (2) a high-concentration electrolyte (HCE) of LiFSI and DME with a molar ratio of 1:1.2; (3) a localized high-concentration electrolyte (LHCE) formed by adding bis(2,2,2-trifluoroethyl) ether (BTFE) diluent into the HCE to yield LiFSI-DME-BTFE = 1:1.2:3 by mole (LHCE-BTFE); and (4) an LHCE with

bis(2,2,2-trifluoroethyl) ether carbonate (BTFEC):LiFSI-DME-BTFEC = 1.0:1.2:3.0 by mole (PLHCE, as free DME molecules are not closely coordinated with Li^+ and making it a pseudo-LHCE[40]) (Supplementary Tables 1 and 2).

The $I-V$ curves of SEIs formed on Cu and Li with the four different electrolytes are shown in Fig. 3. Due to the very thin nature of the SEI (nanoscale), before deciphering the physical meaning of the measured $I-V$ curves of the SEIs, we calibrated the measurement of the $I-V$ curves with known materials at nanoscale as a standard. Therefore, we measured the $I-V$ curves of SiO_2 as a typical insulator and TiO_2 as a semiconductor. As shown in Fig. 3a, even at nanoscale, the $I-V$ curve of SiO_2 shows typical features of an insulator, while that of TiO_2 is a semiconductor. It is rather apparent that the $I-V$ curves of SEIs on both Cu and Li are similar to that of TiO_2 but distinctively different from that of SiO_2, revealing that the electrical properties of SEIs resemble that of a semiconductor. As detailed in Methods and Supplementary Figs. 29-38, based on the results of AIMD simulation of SEI formation and the calculated electronic structure of these four electrolytes, we calculated $I-V$ curve of the SEI on Li metal using the Generalized Electron Nano-Interface Program (GENIP)[13,41]. The calculated $I-V$ curves (Fig. 3d) exhibit similar characteristics and trends to those of experimentally captured ones.

Two characteristic parameters can be extracted from the $I-V$ curves to quantitatively interpret the $I-V$ curves. One is the differential conductance, dI/dV, which is plotted as a function of applied voltage, V (Fig. 3e-h). Another one is the critical field strength for the breakdown of the SEI. The differential conductance of all samples unanimously shows a linear relationship with the applied voltage. However, the slopes of the linear relationship, which can be termed as the rate of differential conductance, are notably different for different samples. It would be expected that for an insulator, such as SiO_2, the $dI/dV-V$ should have a slope of close to zero, which is consistently supported by what we have measured (SiO_2: 6.06×10^{-27} S V^{-1}). For a semiconductor such as TiO_2, the $dI/dV-V$ plot exhibits a positive slope (2.19×10^{-8} S V^{-1}). The differential conductance (dI/dV) of all SEIs on both Cu and Li shows linear positive correlations to the applied voltage, while the values of slopes follow a decreasing order from LCE (3.86×10^{-7} S V^{-1} and 2.72×10^{-7} S V^{-1}) to PLHCE (1.22×10^{-7} S V^{-1} and 2.26×10^{-7} S V^{-1}), HCE (8.93×10^{-8} S V^{-1} and 2.53×10^{-8} S V^{-1}) and LHCE (7.67×10^{-8} S V^{-1} and 1.48×10^{-8} S V^{-1}), where the values in the parentheses correspond to the slopes of $dI/dV-V$ on Cu and Li, respectively. Because the differential conductance represents the electron density of state at the local position of the SEI, the positive linear relationship between dI/dV and voltage indicates that the electrical conductance increases with increasing voltage, implying that the formation of the SEI during battery cycling shows dependence on the voltage difference between the electrode/SEI interface and the SEI/electrolyte interface. The larger the rate of the differential conductance against voltage is, the stronger the SEI responds to the voltage increase. As illustrated in Fig. 3f,g, regardless of the type of substrate (Cu or Li), the SEIs formed by LHCE and HCE electrolytes show a much lower rate of differential conductance than those by PLHCE and LCE electrolytes. The $dI/dV-V$ plot derived from the calculated $I-V$ curve (Fig. 3h) corroborates our experimental results. It should be noted that to account for the SEI thickness effect, we draw the differential conductance,

dI / dV, as a function of the electrical field strength (voltage divided by the thickness of the SEI) by which the SEI thickness effect is normalized as detailed in the Supplementary Note 4. As shown in Supplementary Fig. 15c, the electrical differential conductance against the electrical field strength shows a similar trend of variation for the case of dI / dV as a function of V (Supplementary Fig. 15b).

With increasing the voltage, the current increases parabolically; and to a critical voltage, the current reaches a critical value that exceeds the maximum value of the instrument (Fig. 3). When applying constant voltage above the critical voltage, the current keeps saturated, indicating the transition from semiconductor to conductor is irreversible (Supplementary Fig. 7). Critical field strength is defined as the critical voltage divided by the sample thickness. The critical field strengths of the SEIs for the four electrolytes are different, which correlate positively with the slopes of the $dI / dV - V$ plots as depicted in Fig. 3f,g. The critical field strength of the SEI formed in LHCE is larger than those of SEIs formed in LCE and PLHCE, indicating the SEI formed in LHCE is much stable against increasing voltage as compared with those formed in other three electrolytes.

To demonstrate the direct correlation between the SEI electrical property and battery performance, the electrochemical performances in terms of Coulombic efficiency (CE) and cycle life of those four electrolytes were evaluated in Li||Cu cells and Li||$LiNi_{0.8}Mn_{0.1}Co_{0.1}O_2$ (NMC811) batteries. As shown in Fig. 3i,j, the first cycle CEs of Li||Cu cells and the stable cycle numbers of Li||NMC811 cells have the following orders: LHCE > HCE > PLHCE > LCE (Supplementary Table 3). Overall, an increased differential conductance of the SEI correlates to a decreased Li CE and battery cycling stability (Fig. 3i,j), indicating the governing role of the SEI electrical property on the battery performance.

Correlation of Li morphology with SEI characteristics

Consistent with the above electrochemical property differences among these four electrolytes is the noticeable difference of morphological features of both the SEI and the deposited Li. The deposited Li in these four electrolytes exhibits crystalline structure and granular morphology (Supplementary Figs. 16 and 17). However, the particle size distributions and topographic features vary obviously. Figure 4a shows the morphologies of the deposited Li particles using high angle annular dark field imaging (HAADF) in scanning transmission electron microscope (STEM) by which the image intensity is proportional to the square of atomic number of the sample. The elemental compositions of the SEI, such as O, C, F, S and N, each have a larger atomic number than Li, leading to a large contrast between the SEI and Li, therefore lending the convenience of delineating the spatial distribution of the SEI. On the basis of the SEI configuration maps (Fig. 4b) derived from the STEM-HAADF images (Fig. 4a), it can be seen that the SEI with a high rate of differential conductance corresponds with a high SEI:Li metal ratio.

Three-dimensional (3D) visualization of Li deposits (Supplementary Video 1) yields details of Li topography. It is evident that for the SEI with a high rate of differential conductance and a low critical field strength, as representatively shown for the case of LCE (Fig. 4c), the deposited Li particles exhibit a wide size distribution, a large fraction of isolated small

particles (possible ‘dead’ Li) and a high topographical tortuosity, leading to the high specific surface area of the SEI. In contrast, for the SEI with a low rate of differential conductance and a high critical field strength, as represented by the case of LHCE (Fig. 4c), the deposited Li particles are large, uniformly distributed and topographically smooth, leading to a low specific surface area of the SEI and less ‘dead’ Li.

Thickening of the SEI is a self-limiting process, which is governed by the electron leakage behaviour of the on-growing SEI. Our observations clearly indicate the SEIs formed on Cu (Supplementary Fig. 18) and Li (Fig. 5a) exhibit a similar trend of increasing thickness with a high rate of differential conductance and low critical field strength of the SEI (Fig. 5b). The SEI formed in LCE has the highest rate of differential conductance and the lowest critical field strength, which is corresponded with an SEI thickness of ~35 nm. The SEI formed in LHCE has the lowest rate of differential conductance and the highest critical field strength, corresponding to an SEI thickness of merely 7.5 nm.

Aiming to gain further insight into the origin of different electrical properties of different SEIs, the compositions of SEIs formed on Cu and Li were analysed by cryo-TEM, energy-dispersive X-ray spectroscopy, electron energy-loss spectroscopy (EELS) and X-ray photoelectron spectroscopy (XPS), as shown in Supplementary Figs. 19-28. Chemically, the SEI is composed of Li as the sole cation, which is balanced by the anions comprised of oxygen (O), sulfur (S), carbon (C), fluorine (F) and nitrogen (N). The SEI with a high O:S ratio tends to exhibit a high rate of differential conductance and a low critical field strength, whereas the SEI with a low O:S ratio leads to a low rate of differential conductance and a high critical field strength. The O:S ratios of the SEIs on Cu and Li follow the order from high to low as LCE (4.91 and 19.81) > PLHCE (2.90 and 7.71) > HCE (0.92 and 1.58) > LHCE (0.78 and 0. 69), where the values in the parentheses correspond to the O:S ratios of SEIs on Cu and Li, respectively. These values exactly follow the tendencies of gradually decreased rate of differential conductance and increased critical field strength (Supplementary Fig. 23). The variation of O:S ratio represents the relative contribution of the solvent and salt anion derived components of the SEI in these electrolytes as discussed in detail in the Supplementary Note 5. This observation clearly demonstrates that salt derived component in the SEI leads to low electrical conductance, while the SEI component derived from solvent yields high electrical conductance.

Molecular insight into electrical properties of SEI

To delineate the critical factors, in particular molecular-level information that controls the electrical properties of the SEI, we built Li–electrolyte interface models to investigate the SEI structure using hybrid AIMD-based simulation (Supplementary Figs. 29-39, Supplementary Tables 4-8 and Supplementary Notes 6-7) and subsequently calculated the electron transport in terms of $I - V$ curve as representatively shown in Fig. 5d for the sampling SEI used for the $I - V$ curve calculation. The concentrations of the various species in the SEI derived based on hybrid AIMD generally agree with the XPS data (Supplementary Table 9). We found that SEIs formed in LCE and PLHCE, which exhibit high electrical conductance (Fig. 3), show greater proportion of organic to inorganic phase as signified by a higher C content (Supplementary Fig. 39), indicating the dominance

of solvent-derived SEI components as what we have experimentally observed. The high proportion of organic components in the SEI will lead to large porosity of the SEI, presence of charged molecular fragments or organic radical species due to incomplete molecular reduction and existence of large amount of dissolved Li ions, which may lead to formation of 'dead' Li as observed experimentally (Fig. 4c). All these collectively contribute to the electron leakage. It should be noticed that the lower concentration of sulfate products in the calculated the SEI, as contrasted with that captured from XPS, energy-dispersive X-ray spectroscopy and EELS, is attributed to the fast reaction rate between FSI^- and Li metal and the difference between the electrolyte to anode (E/A) ratio, which may be lower in the simulations than in the experiment[42]. Indeed, we carried out additional simulation with high E/A ratio (Supplementary Figs. 34-36), which demonstrates increased sulfate products, and the calculated $I - V$ shows similar trend (Supplementary Fig. 37b).

Bandgap is a parameter to reflect electron transition from valance to conduction band, which correlates with the electron tunnelling barrier of the SEI[14,15]. To better understand the electrical properties of the SEI, we measured the bandgaps of the SEI using EELS (Supplementary Fig. 40)[43,44]. The bandgap of the SEI on Li deposit shows two obvious features (Fig. 5c). First, the average bandgap of SEIs follows the increasing order as LCE (1.63 ± 0.12 eV) < PLHCE (1.86 ± 0.13 eV) < HCE (2.03 ± 0.19 eV) < LHCE (2.35 ± 0.14 eV), which corresponds well to the orders of increasing critical field strength and decreasing rate of differential conductance. Second, the bandgaps of SEIs in these four electrolytes show spatial variance from outer to inner SEI with exception of LHCE showing nearly a constant bandgap value across the SEI. It is apparent that the spatial change of bandgap across the SEI thickness direction correlates with the chemical composition variations of the SEI. As shown in Supplementary Fig. 24, the SEI formed in HCE shows a distinctive bilayer structure, where the outer layer has high F intensity, while O distributes near the Li deposit and very few C distributes on the surface of the SEI. The composition difference across the SEI indicates the difference of the electronic environment between the outer layer and the inner layer, hence the difference in the bandgap. The O-rich nature in SEIs consistently accounts for the formation of Li_2O particles in the SEIs in LCE, PLHCE and HCE, while SEIs formed in HCE and LHCE contain S-based components. On the basis of bandgap calculation of SEI components as shown in Supplementary Fig. 41 and previous studies[17,18,45,46], it has been indicated that the electron leakage resistance of amorphous Li_2S (3.07 eV) is higher than that of Li_2O (2.2eV) (ref. 46). Furthermore, grain boundaries of inorganic compounds have been predicted to enhance electron tunnelling in the SEI[17,18]. It should be noted that the classic model of the SEI is composed of an inner layer of inorganic and an outer layer of organic[5], which, in terms of electrical properties, correspond to a tandem structure. Apparently, it would be expected that the inner layer of inorganic will be the determining layer on the electrical properties. However, given the fact that the inner layer of the SEI is a composite structure with crystalline particles dispersed in the amorphous matrix (including organic and inorganic species) (Fig. 5a and Supplementary Fig. 19), the electron leakage characteristic will be determined by the continuous amorphous matrix, rather than the dispersed crystalline particles.

Discussion

An ideal SEI is highly ionically conductive but electrically insulative. Our direct measurement of the electrical properties of the SEI reveals the electrical behaviours of SEIs formed in four typical electrolytes. Contrary to what has been conventionally assumed, SEIs do not act as perfect electrical insulators. Instead, they show non-negligible electrical conductance, which governs the SEI formation and Li deposition and consequently affects battery performance. A higher electrical conductance of the SEI could facilitate electron transport inside the SEI, especially at the initial stage of SEI formation, leading to the reduction of Li^+ in the SEI and the formation of metallic Li inside the SEI (Supplementary Fig. 42). This reduced Li is isolated by the SEI, leading to the formation of 'dead' Li and moss Li[47,48]. The 'dead' Li and repeated formation of the SEI give rise to low CE, accounting for why Li CE is much lower in LCE and PLHCE (Fig. 3i). The SEI with high electrical conductance and low critical field strength is more susceptible to local electric field variation, such as that induced by protuberances of Cu surface. If the local electric field strength is higher than the critical field strength of the SEI, localized high electrical conduction will lead to localized Li^+ reduction with or on the surface of the SEI and/or localized thickening of the SEI. The electrical behaviours of the SEI, including electrical conductance and critical field strength, account for their surface uniformity and topographical features.

Nucleation and growth of the SEI are mainly based on the electron tunnelling model, consisting of reduction products of electrolytes formed through the reactions between the electrode and the electrolyte[4-6,12,14,49,50]. Associated with the critical thickness for electron tunnelling, the growth of the SEI would be expected to be self-limiting to a thickness of 2–3 nm (refs. 14,45), which is apparently far deviated from experimentally determined values of ranging from 6 nm to 50 nm (refs. 35,36,38,51,52). The mechanism for further growth beyond the critical tunnelling thickness of 2–3 nm remains elusive. Several mechanisms were proposed to account for SEI growth, that is, electron diffusion through point defects such as Li interstitials[22], solvent diffusion[20,21], electron conduction through the SEI[20,21,26] and transition metal-enabled electron transfer[24]. The voltage-dependent electron leakage mechanism has been included in many battery life models and appears to be the only one to explain some experimental observations[6,14,20-22]. The electrical properties of the SEI are determined by the microstructure and chemistry of SEI components formed by the reduction and reaction of electrolyte solvent and Li salt; the SEI with high content of inorganic spices shows good electrical insulation. Tailoring of electrolyte through compositional optimization towards desired properties for different battery systems offers plenty of room for further research, especially those from machine learning approaches, which could be integrated to delineate the critical component and proper electrolyte chemistry to realize ideal SEI properties, that is, high ionic conductivity and electronic insulation, thus solving major challenges of battery research[53].

Conclusions

We developed an in situ bias TEM method to measure the electrical properties of beam-sensitive SEIs formed on the Cu and Li substrates. Our results reveal that the SEI deviates

from an insulator, showing voltage-dependent differential conductance. A slight variation in the rate of differential conductance can result in dramatic differences in the SEI thickness and Li morphology and, consequently, the electrochemical performance of the batteries. This work provides a direct method to quantify the electrical properties of the SEI and their effects on the electrochemical performances of rechargeable Li-based batteries. The method established here can be generally used for other types of electrochemical cell as well.

Methods

Fabrication and assembly of coin cells

CR2032 Li||Cu coin cells (MTI) were assembled inside an argon (Ar)-filled glovebox. A Cu wire or Cu TEM half grid placed on a Cu foil current collector was used as the working electrode; a Li metal foil was utilized as both the reference electrode and counter electrode. A polyethylene separator (Asahi Kasei) was employed to physically separate the working electrode and the reference/counter electrode. Four electrolytes with the same Li salt LiFSI and solvating solvent DME were prepared in the glovebox: LCE of 1 M LiFSI in DME (with a molar ratio of 1:9), HCE of LiFSI-1.2DME (by molar ratio), LHCEs by diluting the HCE with BTFE diluent to form LHCE and BTFEC to form PLHCE with a molar ratio of 1:1.2:3. The physical properties of those solvents and corresponding electrolytes are summarized in Supplementary Tables 1 and 2. SEI formation on Cu electrode was conducted by applying a current density of 0.1 mA cm^{-2} until the cell reached 0 V. Li metal (that is, the SEI on Li) was electrochemically deposited on Cu with a current density of 0.1 mA cm^{-2} for 100 min to reach a fixed Li deposition amount of an areal capacity of 0.167 mAh cm^{-2} as shown in Supplementary Fig. 1 (by using Arbin BT-2000). Therefore, the SEIs we studied are the ones after the first discharge process.

In situ bias TEM measurement of the electrical property of the SEI

In situ measuring the electrical transport properties of the SEI was conducted inside TEM using a nanofactory holder. The TEM holder features a dual-probe design, comprising two distinct components. One probe utilizes a W probe as the electrode, while the other probe consists of a Cu wire coated with the SEI. The Cu wire probe is movable within the TEM column and is driven by a piezo motor with a 1-nm-step size. Inside an Ar-filled glovebox, the Cu wire with SEI/Li particles formed on it was taken out from the coin cell and affixed on the TEM holder. The TEM holder with airtight cover and sealed within the Ar-filled bag was transferred and inserted into the TEM column. This process ensured limited exposure to air, safeguarding the integrity of the samples and maintaining the desired experimental conditions.

Simulations of SEI formation in each electrolyte

Our simulations follow the recently introduced hybrid ab initio and reactive force field (HAIR) method[54]. This approach uses the AIMD and the reactive force field (ReaxFF) method to extend the time simulation window to the order of hundreds of picoseconds[42]; the AIMD method runs for about 0.5 ps each time to provide an accurate description of the localized electrochemical reactions while the ReaxFF runs for 5 ps, allowing access

to chemical reactions of greater scope and duration, as well as broader mass transfer processes[42].

The Vienna Ab Initio Simulation Package (VASP, version 5.4.4) is used for the AIMD simulation[55]. The Perdew–Burke–Ernzerhof makes the exchange-correlation energy approximation. The projector augmented wave method addresses electron interactions with a plane-wave basis expansion to 400 eV. The Monkhorst–Pack scheme samples the 1×1×1 Brillouin zone, and the occupation method is Gaussian smearing (0.05 eV)[42,56]. The electronic self-consistent convergence criterion is 10^{-4} eV, the ensemble of choice is the NVT and the integration of Newton's equations is with the Verlet algorithm. The hydrogen mass is changed to its tritium isotope to enable a time step of 1.2 fs (ref. 57).

The ReaxFF runs with the large-scale atomic/molecular massively parallel simulation software (LAMMPS, version 3Mar20)[42,56]. The ReaxFF parameterization of choice correctly describes the interfacial interactions between the different organic solvents, the FSI^- anions and the Li surface. The time step is 0.25 fs, the NVT ensemble applies and the Nose–Hoover thermostat has a damping parameter of 0.01 fs^{-1}.

We performed simulations with different length and timescale. The first-round simulations complete 46 HAIR cycles for a total of 253 ps with electrolyte to anode (E/A) ratio of 0.75. The second-round simulations complete 46 HAIR cycles but with larger E/A ratio (2.79). All simulation cells were run with about 450 atoms. To confirm our simulation window is long and large enough to allow the system equilibration, we performed additional simulation with 572 atoms, keeping constant the E/A ratio (0.75) and found no notable structural changes (Supplementary Fig. 36e). We also ran another two simulations up to 1 ns (181 HAIR cycles) and found no notable structural changes (Supplementary Fig. 36d,f). The SEI simulation parameters are summarized in Supplementary Table 4. The details of simulation systems are in Supplementary Note 7 (methodology on SEI layer simulation and subsequently $I - V$ curve calculation).

Current–voltage characteristics of SEI

A fully ab initio DFT with a Green's function approach is used to determine the $I - V$ characteristics of the SEI produced by the four electrolytes in a Li metal anode. The electronic structure of eight SEIs (two per electrolyte taken from hybrid AIMD runs) was obtained using DFT with the hybrid functional B3PW91[58] encoded in the Gaussian-16 programme[59]. The density and superposition matrices of these calculations were entered into the GENIP[13,41] to obtain the $I - V$ characteristics of the 11 samples reported in this work.

3D image reconstruction

Serial tilt HAADF/BF-STEM images were acquired from −60° to 60° by every 2° for 3D reconstruction. The tilt series of whole micrographs were initially aligned using the image processing, modelling and display programme[60], and then reconstructed by the individual particle electron tomography (IPET) method[61]. Final 3D maps were reduced missing-wedge artefact by low-tilt tomographic 3D reconstruction method[62]. All IPET 3D reconstructions

were Gaussian filtered at the same level and rendered in University of California San Francisco Chimera software[63].

Supplementary Material

Refer to Web version on PubMed Central for supplementary material.

Acknowledgements

We thank Y. Wu at Pacific Northwest National Laboratory (PNNL) for providing the TiO_2 sample and C. Yan at University of Chicago for helpful discussions about electrical measurement. This work was supported by the Energy Efficiency and Renewable Energy, Office of Vehicle Technologies of the US Department of Energy (DOE) under the Advanced Battery Materials Research (BMR) Program and the US–Germany Cooperation on Energy Storage under Contract DE-LC-000L072 (C.W. and W.X.). P.B.B. and J.M.S. acknowledge the US–Germany Cooperation on Energy Storage under Contract DE-AC02-05CH11357 and the Assistant Secretary for Energy Efficient and Renewable Energy, Office of Vehicle Technologies of the US DOE through the BMR Program (Battery500 Consortium phase 2) under DOE contract DE-AC05-76RL01830 from PNNL. Computational resources from the Texas A&M University High Performance Research Computing are gratefully acknowledged. The characterization work was conducted in the William R. Wiley Environmental Molecular Sciences Laboratory, a national scientific user facility sponsored by DOE's Office of Biological and Environmental Research and located at PNNL. PNNL is operated by Battelle for the US DOE under contract DE-AC05-76RL01830. The work at the molecular foundry, Lawrence Berkeley National Laboratory was supported by the Office of Science, Office of Basic Energy Sciences of the US DOE under contract DE-AC02-05CH11231. G.R. and J.L. acknowledge US National Institutes of Health grants R01HL115153, R01GM104427, R01MH077303 and R01DK042667.

Data availability

All data that support the findings of this study have been included in this article and its Supplementary Information. Source data are provided with this paper.

References

1. Xu K. Electrolytes and interphases in Li-ion batteries and beyond. Chem. Rev 114, 11503–11618 (2014). [PubMed: 25351820]
2. Cheng XB, Zhang R, Zhao CZ & Zhang Q Toward safe lithium metal anode in rechargeable batteries: a review. Chem. Rev 117, 10403–10473 (2017). [PubMed: 28753298]
3. Lin DC, Liu YY & Cui Y Reviving the lithium metal anode for high-energy batteries. Nat. Nanotechnol 12, 194–206 (2017). [PubMed: 28265117]
4. Peled E. The electrochemical behavior of alkali and alkaline-earth metals in non-aqueous battery systems—the solid–electrolyte-interphase model. J. Electrochem. Soc 126, 2047–2051 (1979).
5. Peled E & Menkin S Review—SEI: past, present and future. J. Electrochem. Soc 164, A1703–A1719 (2017).
6. Wang A, Kadam S, Li H, Shi S & Qi Y Review on modeling of the anode solid–electrolyte interphase (SEI) for lithium-ion batteries. npj Comput. Mater 4, 15 (2018).
7. Xu K. Interfaces and interphases in batteries. J. Power Sources 559, 232652 (2023).
8. Ma YG et al. Structure and reactivity of alucone-coated films on Si and Li_xSi_y surfaces. ACS Appl. Mater. Inter 7, 11948–11955 (2015).
9. Wang LN et al. Identifying the components of the solid–electrolyte interphase in Li-ion batteries. Nat. Chem 11, 789–796 (2019). [PubMed: 31427766]
10. Shen X. et al. The failure of solid–electrolyte interphase on Li metal anode: structural uniformity or mechanical strength? Adv. Energy Mater 10, 1903645 (2020).
11. Winter M. The solid–electrolyte interphase—the most important and the least understood solid electrolyte in rechargeable Li batteries. Z. Phys. Chem 223, 1395–1406 (2009).
12. He X. et al. The passivity of lithium electrodes in liquid electrolytes for secondary batteries. Nat. Rev. Mater 6, 1036–1052 (2021).

13. Benitez L & Seminario JM Electron transport and electrolyte reduction in the solid–electrolyte interphase of rechargeable lithium-ion batteries with silicon anodes. J. Phys. Chem. C 120, 17978–17988 (2016).
14. Lin YX et al. Connecting the irreversible capacity loss in Li-ion batteries with the electronic insulating properties of solid–electrolyte-interphase (SEI) components. J. Power Sources 309, 221–230 (2016).
15. Liu Z. et al. Interfacial study on solid–electrolyte interphase at Li metal anode: implication for Li dendrite growth. J. Electrochem. Soc 163, A592–A598 (2016).
16. Zhang QL et al. Synergetic effects of inorganic components in solid–electrolyte interphase on high cycle efficiency of lithium-ion batteries. Nano Lett. 16, 2011–2016 (2016). [PubMed: 26889564]
17. Feng M, Pan J & Qi Y Impact of electronic properties of grain boundaries on the solid-electrolyte interphases (SEIs) in Li-ion batteries. J. Phys. Chem. C 125, 15821–15829 (2021).
18. Smeu M & Leung K Electron leakage through heterogeneous LiF on lithium metal battery anodes. Phys. Chem. Chem. Phys 23, 3214–3218 (2021). [PubMed: 33533339]
19. Christensen J & Newman J A mathematical model for the lithium-ion negative electrode solid–electrolyte interphase. J. Electrochem. Soc 151, A1977–A1988 (2004).
20. Single F, Horstmann B & Latz A Dynamics and morphology of solid-electrolyte interphase (SEI). Phys. Chem. Chem. Phys 18, 17810–17814 (2016). [PubMed: 27327841]
21. Single F, Horstmann B & Latz A Revealing SEI morphology: in-depth analysis of a modeling approach. J. Electrochem. Soc 164, E3132–E3145 (2017).
22. Single F, Latz A & Horstmann B Identifying the mechanism of continued growth of the solid–electrolyte interphase. ChemSusChem 11, 1950–1955 (2018). [PubMed: 29528554]
23. Kobbing L, Latz A & Horstmann B Growth of the solid–electrolyte interphase: electron diffusion versus solvent diffusion. J. Power Sources 561, 232651 (2023).
24. Harris OC, Lin YX, Qi Y, Leung K & Tang MH How transition metals enable electron transfer through the SEI: part I. Experiments and Butler–Volmer modeling. J. Electrochem. Soc 167, 013502 (2019).
25. Ploehn HJ, Ramadass P & White RE Solvent diffusion model for aging of lithium-ion battery cells. J. Electrochem. Soc 151, A456–A462 (2004).
26. Attia PM, Das S, Harris SJ, Bazant MZ & Chueh WC Electrochemical kinetics of SEI growth on carbon black: part I. Experiments. J. Electrochem. Soc 166, E97–E106 (2019).
27. Tang M, Lu SD & Newman J Experimental and theoretical investigation of solid–electrolyte-interphase formation mechanisms on glassy carbon. J. Electrochem. Soc 159, A1775–A1785 (2012).
28. Riess I. Four point Hebb–Wagner polarization method for determining the electronic conductivity in mixed ionic–electronic conductors. Solid State Ionics 51, 219–229 (1992).
29. Liu Y. et al. Impacts of the properties of anode solid–electrolyte interface on the storage life of Li-ion batteries. J. Phys. Chem. C 122, 9411–9416 (2018).
30. Lorger S, Usiskin R & Maier J Transport and charge carrier chemistry in lithium oxide. J. Electrochem. Soc 166, A2215–A2220 (2019).
31. Stetson C. et al. Three-dimensional electronic resistivity mapping of solid–electrolyte interphase on Si anode materials. Nano Energy 55, 477–485 (2019).
32. Santos CS, Botz A, Bandarenka AS, Ventosa E & Schuhmann W Correlative electrochemical microscopy for the elucidation of the local ionic and electronic properties of the solid–electrolyte interphase in Li-ion batteries. Angew. Chem. Int. Ed 61, e202202744 (2022).
33. Su Y. et al. LiPON thin films with high nitrogen content for application in lithium batteries and electrochromic devices prepared by RF magnetron sputtering. Solid State Ion. 282, 63–69 (2015).
34. Han F. et al. High electronic conductivity as the origin of lithium dendrite formation within solid electrolytes. Nat. Energy 4, 187–196 (2019).
35. Li YZ et al. Atomic structure of sensitive battery materials and interfaces revealed by cryo-electron microscopy. Science 358, 506–510 (2017). [PubMed: 29074771]

36. Wang XF et al. New insights on the structure of electrochemically deposited lithium metal and its solid–electrolyte interphases via cryogenic TEM. Nano Lett. 17, 7606–7612 (2017). [PubMed: 29090936]
37. Zachman MJ, Tu Z, Choudhury S, Archer LA & Kourkoutis LF Cryo-STEM mapping of solid–liquid interfaces and dendrites in lithium metal batteries. Nature 560, 345–349 (2018). [PubMed: 30111789]
38. Xu Y. et al. Atomic to nanoscale origin of vinylene carbonate enhanced cycling stability of lithium metal anode revealed by cryo-transmission electron microscopy. Nano Lett. 20, 418–425 (2020). [PubMed: 31816244]
39. Ren X. et al. Role of inner solvation sheath within salt–solvent complexes in tailoring electrode/electrolyte interphases for lithium metal batteries. Proc. Natl Acad. Sci. USA 117, 28603–28613 (2020). [PubMed: 33144505]
40. Cao X. et al. Effects of fluorinated solvents on electrolyte solvation structures and electrode/electrolyte interphases for lithium metal batteries. Proc. Natl Acad. Sci. USA 118, e2020357118 (2021). [PubMed: 33632763]
41. Derosa PA & Seminario JM Electron transport through single molecules: scattering treatment using density functional and green function theories. J. Phys. Chem. B 105, 471–481 (2001).
42. Beltran SP & Balbuena PB SEI formation mechanisms and Li^+ dissolution in lithium metal anodes: impact of the electrolyte composition and the electrolyte-to-anode ratio. J. Power Sources 551, 232203 (2022).
43. Rafferty B & Brown LM Direct and indirect transitions in the region of the bandgap using electron-energy-loss spectroscopy. Phys. Rev. B 58, 10326–10337 (1998).
44. Liu X. et al. Local electronic structure variation resulting in Li ‘filament’ formation within solid electrolytes. Nat. Mater 20, 1485–1490 (2021). [PubMed: 34059815]
45. Li YS & Qi Y Transferable self-consistent charge density functional tight-binding parameters for Li-metal and Li-ions in inorganic compounds and organic solvents. J. Phys. Chem. C 122, 10755–10764 (2018).
46. Xu JG et al. Mechanical and electronic stabilization of solid–electrolyte interphase with sulfite additive for lithium metal batteries. J. Electrochem. Soc 166, A3201–A3206 (2019).
47. Lu DP et al. Failure mechanism for fast-charged lithium metal batteries with liquid electrolytes. Adv. Energy Mater 5, 1400993 (2015).
48. Fang C. et al. Quantifying inactive lithium in lithium metal batteries. Nature 572, 511–515 (2019). [PubMed: 31435056]
49. Peled E, Golodnitsky D & Ardel G Advanced model for solid–electrolyte-interphase electrodes in liquid and polymer electrolytes. J. Electrochem. Soc 144, L208–L210 (1997).
50. Aurbach D. et al. New insights into the interactions between electrode materials and electrolyte solutions for advanced non-aqueous batteries. J. Power Sources 81, 95–111 (1999).
51. Zhang Z. et al. Capturing the swelling of solid-electrolyte interphase in lithium metal batteries. Science 375, 66–70 (2022). [PubMed: 34990230]
52. Yu Z. et al. Molecular design for electrolyte solvents enabling energy-dense and long-cycling lithium metal batteries. Nat. Energy 5, 526–533 (2020).
53. Li J. et al. Dynamics of particle network in composite battery cathodes. Science 376, 517–521 (2022). [PubMed: 35482882]
54. Liu Y. et al. The DFT-ReaxFF hybrid reactive dynamics method with application to the reductive decomposition reaction of the TFSI and DOL electrolyte at a lithium metal anode surface. J. Phys. Chem. Lett 12, 1300–1306 (2021). [PubMed: 33502211]
55. Kresse G & Hafner J Ab initio molecular dynamics for liquid metals. Phys. Rev. B 47, 558–561 (1993).
56. Plimpton S. Fast parallel algorithms for short-range molecular dynamics. J. Comput. Phys 117, 1–19 (1995).
57. Kamphaus EP & Balbuena PB First-principles investigation of lithium polysulfide structure and behavior in solution. J. Phys. Chem. C 121, 21105–21117 (2017).

58. Perdew JP & Wang Y Accurate and simple analytic representation of the electron-gas correlation energy. Phys. Rev. B 45, 13244–13249 (1992).

59. Frisch MJ et al. Gaussian 16 Rev. C.01 (Gaussian, 2016).

60. Kremer JR, Mastronarde DN & McIntosh JR Computer visualization of three-dimensional image data using IMOD. J. Struct. Biol 116, 71–76 (1996). [PubMed: 8742726]

61. Zhang L & Ren G IPET and FETR: experimental approach for studying molecular structure dynamics by cryo-electron tomography of a single-molecule structure. PLoS ONE 7, e30249 (2012). [PubMed: 22291925]

62. Zhai XB et al. LoTToR: an algorithm for missing-wedge correction of the low-tilt tomographic 3D reconstruction of a single-molecule structure. Sci. Rep 10, 10489 (2020). [PubMed: 32591588]

63. Pettersen EF et al. UCSF chimera—a visualization system for exploratory research and analysis. J. Comput. Chem 25, 1605–1612 (2004). [PubMed: 15264254]

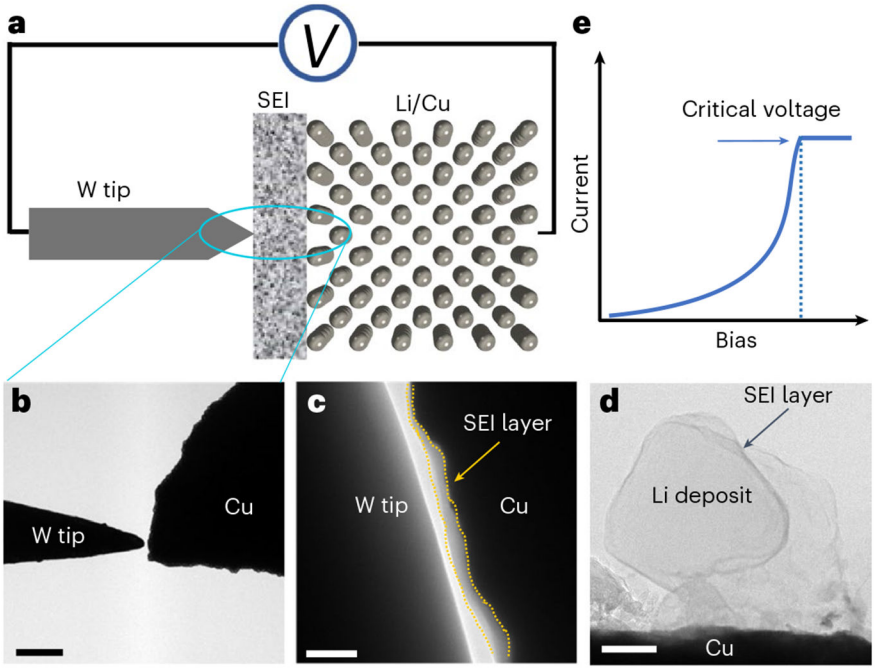

Fig. 1 | In situ bias TEM measurement of electrical properties of the SEI.

a, Schematic of experiment set-up. **b**. Low-magnification TEM image showing in situ bias set-up of W tip and Cu wire inside TEM. **c**, High-magnification TEM image showing contact between W tip and Cu wire with the SEI on the Cu. **d**, TEM image showing Li deposit with the surface SEI layer using Cu wire as electrode. **e**, Typical $I - V$ curves showing the critical voltage. Scale bars, 50 μm in (**c**) and 100 nm in (**b**,**d**).

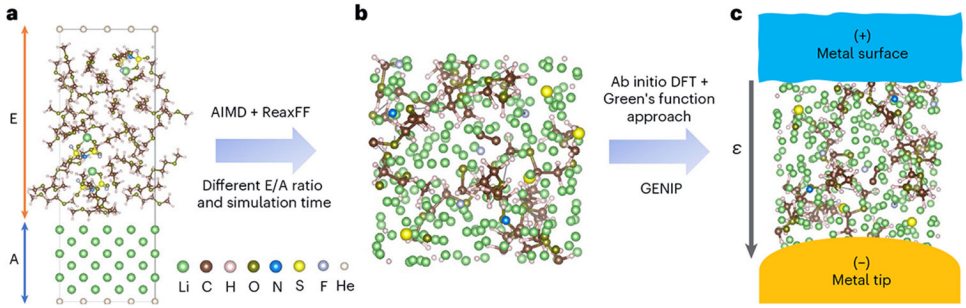

Fig. 2 | Simulation of the SEI structure and subsequent calculation of $I - V$ curve.
a, Simulation cell with different E/A ratio. **b**, Final states of the SEI formed by reaction between electrolyte and Li metal with different E/A ratio and simulation time via AIMD and ReaxFF method. **c**, Schematic of $I - V$ curve calculation set-up of simulated SEI via ab initio DFT with a Green's function approach. ε, voltage.

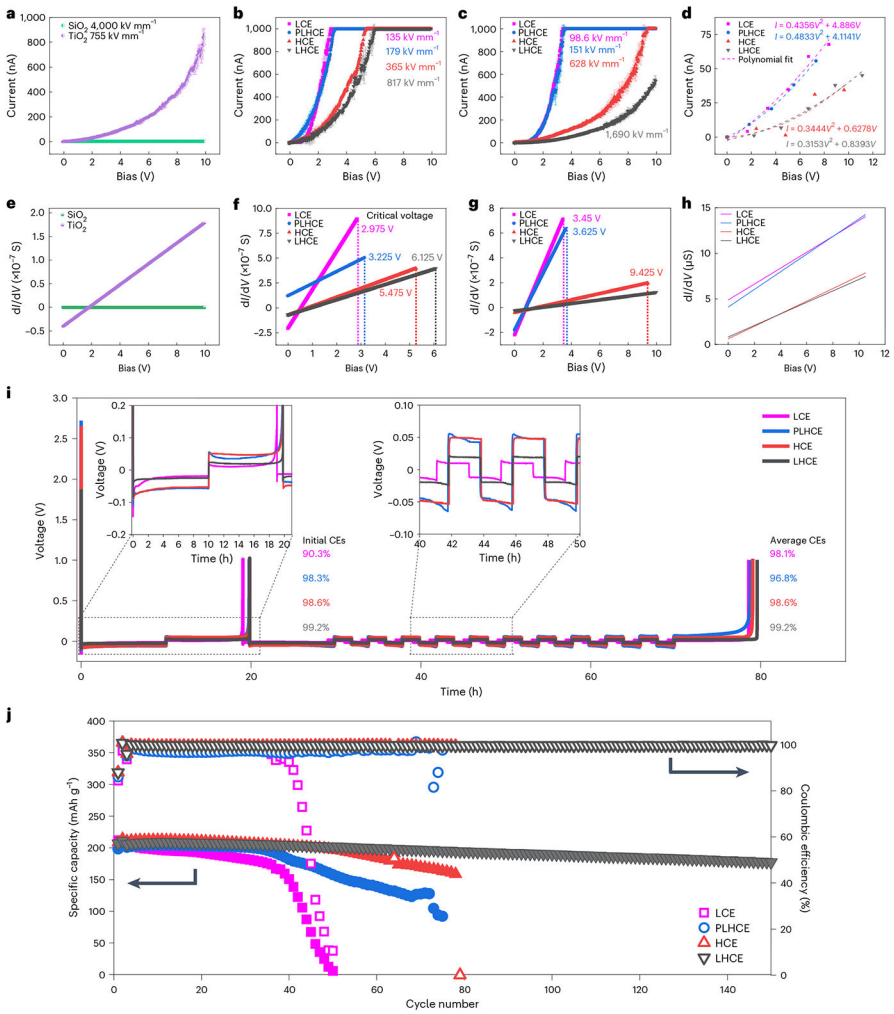

Fig. 3 | Electrical properties of SEI and electrochemical cell performances.

a, $I - V$ curves of SiO_2 insulator and TiO_2 semiconductor. Error bars are s.d.; $n = 10$. **b**, $I - V$ curves of the SEI formed on Cu. **c**, $I - V$ curves of the SEI formed on Li deposits. Error bars are s.d.; $n = 10$. **d**, Calculated $I - V$ curve based on sample cell (E/A ratio is 2.79, simulation time is 253 ps). **e**–**h**, Differential conductance, dI / dV as function of V, derived from the $I - V$ curves, with the critical voltage indicated, for SiO_2 and TiO_2 (**e**), for SEI on Cu (**f**), for SEI on Li (**g**) and for calculated SEI on Li (**h**). The slope of the dI / dV against V in **d**–**f** is termed as rate of differential conductance. **i**, CE of Li||Cu cells. Left inset: CE curve at higher magnification of the initial 20 h. Right inset: CE curve at higher magnification from 40 h to 50 h. Average CEs are from ten cycles. **j**, Long-term cycling stability of Li||NMC811 cells in LCE, PLHCE, HCE and LHCE electrolytes. Error bars in (**a**–**c**) show the reproducibility of measured $I - V$ curves.

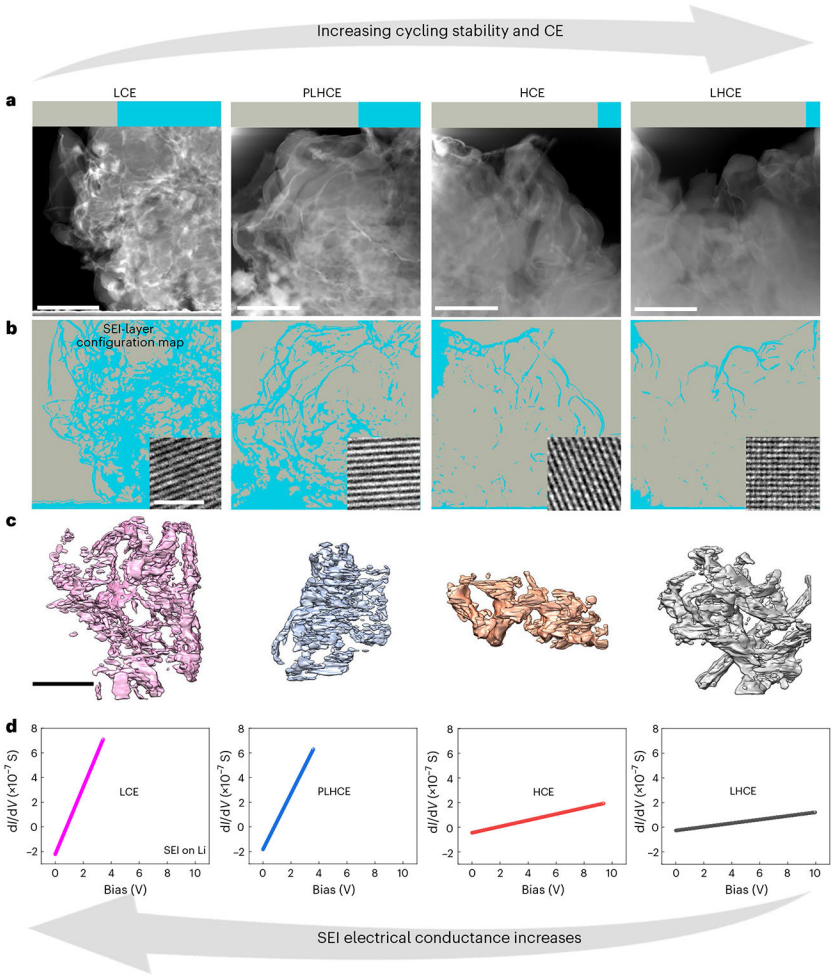

Fig. 4 |. Dependence of microstructure of Li deposits on rate of differential conductance.

a, Low-magnification cryo-STEM-HAADF images of Li deposits formed in LCE, PLHCE, HCE and LHCE; grey and blue bars indicate the area fraction of Li and SEI, respectively. **b**, SEI-layer configuration maps derived from the STEM-HAADF images. Insets: high-resolution TEM images of Li deposits. **c**, Three-dimensional reconstruction of Li deposits. **d**, $dI / dV - V$ curves of the SEI on Li formed in those four electrolytes, where the slope of dI / dV as a function of V is termed as rate of differential conductance. Scale bars, 5 μm in (**a**,**c**) and 5 nm (inset in **b**).

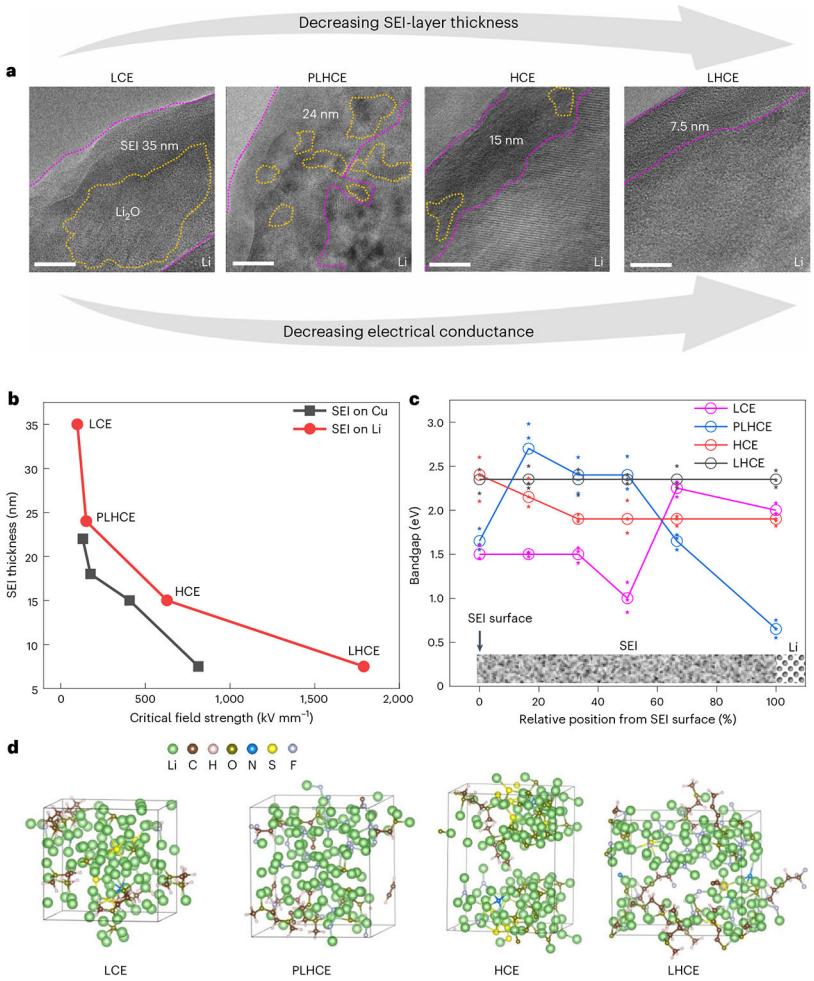

Fig. 5 | Correlation between SEI structure and its electrical property.

a, Atomic structure of SEI layers on the Li deposits formed in LCE, PLHCE, HCE and LHCE. Scale bars, 5 nm. **b**, SEI thickness as a function of the critical field strength of the SEI on Cu and Li, indicating the SEI layer thickness decreases with increasing critical field strength. **c**, Measured bandgap of the SEI layer on Li for different electrolytes, demonstrating bandgap decrease from the SEI surface towards Li interface. The stars represent individual data points, and the circle signifies the mean. **d**, Snapshots of samples for four electrolytes reacting with Li metal in $I - V$ curve calculations (E/A ratio is 2.79; simulation time is 253 ps).